The Astrophysical Journal, 974:223 (11pp), 2024 October 20 https://doi.org/10.3847/1538-4357/ad71c4

The Imprint of Dark Matter on the Galactic Acceleration Field

Arpit Arora[1], Robyn E. Sanderson[1], Sukanya Chakrabarti[2], Andrew Wetzel[3], Thomas Donlon II[2], Danny Horta[4], Sarah R. Loebman[5], Lina Necib[6,7], and Micah Oeur[5]
[1] Department of Physics and Astronomy, University of Pennsylvania, 209 South 33rd Street, Philadelphia, PA 19104, USA
[2] Department of Physics and Astronomy, University of Alabama in Huntsville, 301 North Sparkman Drive, Huntsville, AL 35816, USA
[3] Department of Physics & Astronomy, University of California, Davis, CA 95616, USA
[4] Center for Computational Astrophysics, Flatiron Institute, 162 5th Avenue, New York, NY 10010, USA
[5] Department of Physics, University of California, Merced, 5200 Lake Road, Merced, CA 95343, USA
[6] Department of Physics and MIT Kavli Institute for Astrophysics and Space Research, Massachusetts Institute of Technology, 77 Massachusetts Avenue, Cambridge, MA 02139, USA
[7] The NSF AI Institute for Artificial Intelligence and Fundamental Interactions, 77 Massachusetts Avenue, Cambridge, MA 02139, USA
Received 2024 June 18; revised 2024 August 15; accepted 2024 August 19; published 2024 October 15

Abstract

Measurements of the accelerations of stars enabled by time-series extreme-precision spectroscopic observations, pulsar timing, and eclipsing binary stars in the solar neighborhood offer insights into the mass distribution of the Milky Way that do not rely on traditional equilibrium modeling. Given the measured accelerations, we can determine a total mass density and infer the amount of dark matter (DM) by accounting for the mass in stars, gas, and dust. Leveraging FIRE-2 simulations of Milky Way–mass galaxies we compare vertical acceleration profiles between cold DM (CDM) and self-interacting DM (SIDM) with a constant cross section of 1 $cm^2\ g^{-1}$ across three halos with diverse assembly histories. Notably, significant asymmetries in vertical acceleration profiles near the midplane at fixed radii are observed in both CDM and SIDM, particularly in halos recently affected by mergers with satellites of Sagittarius/SMC-like masses or greater. These asymmetries offer a unique window into exploring the merger history of a galaxy. We show that SIDM halos manifest a more oblate shape and consistently exhibit higher local stellar and DM densities and steeper vertical acceleration gradients, up to 10%–30% steeper near the solar neighborhood. However, similar magnitude changes can arise from azimuthal variations in the baryonic components at a fixed radius and external influences like mergers, making it difficult to distinguish between CDM and SIDM using acceleration measurements in a single galaxy.

Unified Astronomy Thesaurus concepts: Galaxy dynamics (591); Dark matter density (354); Dark matter (353)

1. Introduction

Dark matter (DM) constitutes approximately 85% of the matter in the Universe (C. Planck et al. 2020), but its nature remains elusive. The standard cold DM (CDM) model, which assumes that DM particles are collisionless and noninteracting, has been successful in explaining large-scale structures in the Universe. However, there are several inconsistencies at small scales, such as the too-big-to-fail tension, core-cusp tension, planes of satellites, and others (e.g., R. A. Flores & J.R. Primack 1994; B. Moore 1994; B. Moore et al. 1999; J. S. Bullock & M. Boylan-Kolchin 2017; S. Tulin & H. -B. Yu 2018; L. V. Sales et al. 2022).

One unresolved issue is the "diversity of rotation curves," where the observed rotation curves for dwarf satellites and Milky Way (MW)–mass galaxies show a stunning diversity, with inferred inner DM profiles ranging from cored to Navarro–Frenk–White (NFW)–like and even more concentrated than NFW profiles (e.g., K. A. Oman et al. 2015; J. Zavala et al. 2019). On the other hand, CDM simulations predict a steeply rising central density profile, and reproducing such diversity in inner DM profiles remains a challenge even with additions of baryonic components with active feedback (M. G. Walker & J. Penarrubia 2011; I. M. E. Santos-Santos et al. 2020; T. Ebisu et al. 2022).

This discrepancy has spurred exploration into alternative models, such as self-interacting DM (SIDM; E. D. Carlson et al. 1992; D. N. Spergel & P. J. Steinhardt 2000), which allows DM particles to interact with each other through elastic collisions. Such interactions can lead to a transfer of kinetic energy from the hot outer region to the dense inner region, resulting in a more cored density profile (D. N. Spergel & P. J. Steinhardt 2000; N. Yoshida et al. 2000; P. Colin et al. 2002; G. Gentile et al. 2004; S. Tulin & H. -B. Yu 2018; P. Salucci 2019). Moreover, a large self-interaction cross section ($\sigma/m \leqslant 10\ cm^2\ g^{-1}$) can induce a core-collapse phase that drives the DM mass toward the center and forms steeper inner DM profiles (F. Kahlhoefer et al. 2019; J. Zavala et al. 2019; O. Sameie et al. 2020).

Recent studies have shown that SIDM can reproduce some observed properties of dwarf galaxies and MW-mass galaxies better than CDM (M. Vogelsberger et al. 2012, 2019; A. H. G. Peter et al. 2013; M. Rocha et al. 2013), such as their shapes (O. Sameie et al. 2018, 2021; D. Vargya et al. 2022) and inner densities (M. Kaplinghat et al. 2016). One effective test of DM involves measuring the DM mass distribution within a galaxy. The most straightforward and least assumptive method for probing the mass distribution (including stars, gas, and DM) in the Galaxy is through acceleration measurements of stars in the MW. Recent advances in high-precision spectrographs (e.g., D. A. Fischer et al. 2016; C. Schwab et al. 2016; J. T. Wright & P. Robertson 2017; F. Pepe et al. 2021), improving precision in pulsar timing data (e.g., M. J. Keith et al. 2013; T. T. Pennucci 2019;

B. Goncharov et al. 2021), and high-precision spectroscopic observations of eclipsing binary stars by space-based missions (K. G. Hełminiak et al. 2019) now enable direct measurement of Galactic accelerations in the solar neighborhood with multiple independent techniques (e.g., C. Quercellini et al. 2008; H. Silverwood & R. Easther 2019; S. Chakrabarti et al. 2020, 2021, 2022a, 2022b; D. F. Phillips et al. 2021).

Acceleration measurements can be used to determine the shape of the MW potential in the solar neighborhood and constrain the Galactic midplane density (Oort limit; S. Chakrabarti et al. 2020, 2021; T. Donlon et al. 2024), from which we can determine the local DM density after accounting for the baryon budget. Notably, in comparison to alternative methodologies (reviewed comprehensively by P. F. de Salas & A. Widmark 2021), acceleration measurements require far fewer assumptions. Using Poisson's equation, given an acceleration field (i.e., the gradient of the potential), we can straightforwardly determine the local density.

These properties of the MW depend on the DM model (O. Sameie et al. 2018, 2021; D. Vargya et al. 2022), indicating that measurement of the local DM density and the shape of the potential can provide discriminating power for constraining the nature of DM. Prior work on determinations of the Oort limit has focused on kinematic analysis (e.g., P. Salucci et al. 2010; C. F. McKee et al. 2015; K. Schutz et al. 2018; R. Guo et al. 2020; P. F. de Salas & A. Widmark 2021), which models a snapshot in time of the positions and speeds of stars under simplifying assumptions of equilibrium and/or symmetry both across the midplane and axisymmetrically, which can lead to inaccurate inferences of Galactic parameters for a time-dependent potential (T. Haines et al. 2019).

S. Chakrabarti et al. (2020) demonstrated that perturbations from past mergers such as the Gaia–Sausage–Enceladus merger (V. Belokurov et al. 2018; A. Helmi et al. 2018), the Sagittarius dwarf galaxy (R. A. Ibata et al. 1994; K.V. Johnston et al. 1995; H. J. Newberg et al. 2002), the ongoing merger with the LMC (G. Besla et al. 2007; N. Kallivayalil et al. 2013), and other possible disturbances in the MW such as formation of a warped disk (E. C. Ostriker & J. J. Binney 1989; N. W. Evans et al. 1998) or large planar disturbances in the outer gas disk of the Galaxy (S. Chakrabarti & L. Blitz 2009; S. Chakrabarti et al. 2019) can induce asymmetries in the Galactic acceleration profile. These nonequilibrium effects are naturally taken into account while studying DM through direct measurement of Galactic accelerations, because extreme-precision time-series observations of stars provide the Galactic acceleration *today* without assuming equilibrium or symmetry as in kinematic analyses. Moreover, kinematic analyses only yield the average acceleration for a bulk population of stars, which offers less constraining power.

Cosmological simulations with a realistic baryonic disk and assembly history can serve as a natural test laboratory for interrogating tools to measure local DM density (e.g., L. Necib et al. 2019; X. Ou et al. 2024) and for interpreting Galactic acceleration observations (S. R. Loebman et al. 2012, 2014). Moreover, by examining these simulations across different DM models, we can effectively constrain the mass distribution and nature of DM.

In this paper, we use cosmological baryonic simulations with varying merger histories described in Section 2 to analyze their Galactic acceleration fields (Section 3) under different DM models. In Section 2.2, we compare fundamental Galactic parameters, such as the measured shape of the MW potential determined from the time-rate of change of the orbital period of binary pulsars (S. Chakrabarti et al. 2021; T. Donlon et al. 2024), with our simulations. We avoid using the time-rate of change of the spin period (D. F. Phillips et al. 2021) due to large uncertainties caused by the unknown effect of magnetic braking on the spin periods. Our conclusions are presented in Section 4.

2. Simulations of MW-mass Galaxies

We use three MW-mass galaxies using cosmological baryonic simulations from the `Latte` suite (A. Wetzel et al. 2023) of FIRE-2 simulations with initial conditions derived from AGORA (J.-h. Kim et al. 2014) run with `GIZMO` (P. F. Hopkins 2015). The halos labeled m12f, m12i, and m12m are some of the most MW-like isolated disks in the suite and span a range of assembly histories. All the halos use identical baryonic FIRE-2 physics (P. F. Hopkins et al. 2018) and two distinct DM models: CDM, which employs cold-collisionless DM, and SIDM, which adopts SIDM with a cross section of $\sigma/m = 1\,\mathrm{cm}^2\ \mathrm{g}^{-1}$. The SIDM implementation in `GIZMO` (introduced in A. H. G. Peter et al. 2013; M. Rocha et al. 2013) employs a Monte Carlo approach to determine the scattering probability for the nearest neighbors of each DM particle using a spline kernel with adaptive smoothing length (J. J. Monaghan & J. C. Lattanzio 1985). It then assigns velocities isotropically to the scattered particles to conserve energy and momentum. The cross section of $\sigma/m = 1\,\mathrm{cm}^2\,\mathrm{g}^{-1}$ for SIDM is often used for MW-mass galaxies to achieve a balance between addressing small-scale problems (S. Tulin & H. -B. Yu 2018) and maintaining agreement with larger-scale galactic and cluster observations (S. W. Randall et al. 2008).

These halos are all isolated systems with no massive companion halos within 4 Mpc and have a virial mass of approximately $\sim$1–1.5 $\times\ 10^{12}\ M_\odot$. Each simulation uses an initial particle mass of $m_\mathrm{b} = 7100\,M_\odot$ for stars and gas, and $m_\mathrm{DM} = 35{,}000\ M_\odot$ for DM with a minimum physical spatial resolution $\epsilon_\mathrm{gas} = 1$ pc, $\epsilon_\star = 4$ pc, and $\epsilon_\mathrm{DM} = 20$ pc. Also, the potential and acceleration values are tracked for every particle in the simulation.

The properties of the halos, including halo shapes and density profiles, along with a description of the simulation methods, are detailed in O. Sameie et al. (2021) and D. Vargya et al. (2022). These halos are part of a suite of simulations dedicated to exploring alternative DM models that are different from the fiducial FIRE-2 simulations presented in A. Wetzel et al. (2023). In these simulations, any thermal energy to momentum for stellar winds energy conversion resulting from stellar mass-loss processes is neglected for the subresolution regions, which leads to a lower (almost a factor of 2) stellar mass than our fiducial FIRE-2 simulations.

Notably, FIRE-2 CDM halos exhibit MW-like stellar-to-halo mass ratios (P. F. Hopkins et al. 2018), stellar morphologies and kinematics (X. Ma et al. 2017; F. McCluskey et al. 2024), and other properties such as gas fractions, scale radii, scale heights, and satellite populations (e.g., I. Escala et al. 2018; K. El-Badry et al. 2018; R. E. Sanderson et al. 2018; J. Samuel et al. 2021), making them ideal for comparing with observational Galactic accelerations in the solar neighborhood.

Additionally, the three halos have distinct mergers and assembly histories. The simulation m12i features a thick young disk with an intermediate formation epoch (R. E. Sanderson

Table 1
Properties of Simulated Galaxies and Their Azimuthal Variation at the Solar Circle, $R_\odot = 8.1 \pm 0.6$ kpc, Comparing CDM and SIDM Models with the MW at the Present Day

		Halo Property		Surface Density[a] ($M_\odot$ pc^{-2})		Volume Density[b] ($10^{-3}\,M_\odot$ pc^{-3})				Scale Height (pc)		
Galaxy	Physics	$M_\star$ ($M_\odot$)[c]	$r_{1/2}$ (kpc)[c]	Total	Baryonic	Total	Stars	Gas	DM	Stars Thin	Stars Thick	Cold[d] Gas
MW[e]	?	$5^{+0.4}_{-0.5} \times 10^{10}$	4.2^{+1}_{-1}	70^{+5}_{-5}	$43.8^{+3.4}_{-3.4}$	$99.5^{+9.5}_{-9.5}$	42.4^{+3}_{-3}	45.9^{+8}_{-8}	$10.5^{+2.5}_{-2.5}$	300^{+60}_{-60}	900^{+180}_{-180}	150
m12i	CDM	3.4×10^{10}	4.3	44.7^{+24}_{-5}	25.3^{+24}_{-4}	23.1^{+15}_{-11}	$7.8^{+6.3}_{-4.5}$	$6.6^{+8.2}_{-5.8}$	$8.7^{+0.2}_{-0.2}$	566.4	2000[f]	321.5
	SIDM	5.2×10^{10}	3.8	55.9^{+24}_{-17}	36.8^{+23}_{-17}	30.3^{+18}_{-15}	$11.2^{+5.2}_{-4.5}$	10.4^{+13}_{-10}	$9.1^{+0.1}_{-0.1}$	488	1503.4	359.1
m12f	CDM	5.8×10^{10}	3.6	61.1^{+20}_{-13}	39.2^{+19}_{-11}	33.5^{+19}_{-11}	$12.9^{+4.3}_{-3.1}$	$10.4^{+15.2}_{-7.6}$	$10.1^{+0.3}_{-0.3}$	569.9	2000[f]	363.4
	SIDM	6.7×10^{10}	4.7	67.9^{+20}_{-16}	43.4^{+20}_{-16}	35.7^{+22}_{-10}	$16.7^{+5.5}_{-3.2}$	$7.6^{+16}_{-6.4}$	$11.4^{+0.3}_{-0.1}$	437.6	1078.6	322.8
m12m	CDM	5.1×10^{10}	8.2	63.3^{+19}_{-15}	39.6^{+18}_{-15}	35^{+20}_{-10}	$16^{+5.7}_{-2.8}$	$8.3^{+13.2}_{-7.3}$	$10.6^{+0.2}_{-0.2}$	153.3	682	297.6
	SIDM	6.9×10^{10}	8.3	87.9^{30}_{-26}	57^{+29}_{-25}	49.5^{+28}_{-13}	$25^{+8.6}_{-5.4}$	$10.7^{+19}_{-7.4}$	$13.9^{+0.3}_{-0.3}$	218.4	742.9	317.2

Notes. $M_\star$: stellar mass within 10% of the radius where the cumulative density is 200 times the critical density of the Universe. $r_{1/2}$: 3D stellar half-mass radius.
[a] Materials within $|Z| \leqslant 1.1$ kpc.
[b] Materials within $|Z| \leqslant 0.2$ kpc with values from K. Schutz et al. (2018) and P. F. de Salas & A. Widmark (2021). The MW values are consistent within 1 standard deviation with values in C. F. McKee et al. (2015) and J. Bland-Hawthorn & O. Gerhard (2016).
[c] Values from M. Cautun et al. (2020), consistent within 1 standard deviation with values in J. Bland-Hawthorn & O. Gerhard (2016) and MWPotential2022 from GALA (A. M. Price-Whelan 2017).
[d] Gas temperature, $T \leqslant 100$ K.
[e] Values from C. F. McKee et al. (2015) unless noted, consistent within 1 standard deviation with values in J. Bland-Hawthorn & O. Gerhard (2016).
[f] Modeled better with single sech profile. Volume densities remain consistent with changing the width of the solar circle and Z range. Please note that our halo values differ from those in R. E. Sanderson et al. (2020) because our CDM simulations, as noted in Section 2, are different from the fiducial FIRE-2 suite. The error bars in the simulation show the azimuthal variation in low- and high-density regions.

et al. 2020) with a merger with first pericentric passage around 6 Gyr before the present day. m12f had a major merger with a pair of satellites similar in total mass to the progenitor of the Sagittarius stream (I.-G. Jiang & J. Binney 2000; M. Niederste-Ostholt et al. 2010; T. J. L. de Boer et al. 2015; S. Gibbons et al. 2017) with the first pericentric passage about 3 Gyr before the present day (A. Arora et al. 2022; N. Garavito-Camargo et al. 2023). In contrast, m12m is the earliest-forming, has a massive disk, and has no massive mergers in the last 7 Gyr of its evolution (V. P. Debattista et al. 2019). Table 1 lists the total stellar mass within 10% of the virial radius, where the cumulative density is 200 times the critical density of the Universe ($M_\star$) and the 3D stellar half-mass radius ($r_{1/2}$) for all of the galaxies. While the total virial mass of these systems is the same in the SIDM and CDM runs, the SIDM simulations have systematically higher stellar mass throughout the disk due to increased star formation rates at late times (O. Sameie et al. 2021) and larger galaxy sizes, quantified by $r_{1/2}$, compared to the CDM simulations.

2.1. The Solar Neighborhood

Given the cosmological nature of these simulations in an arbitrary comoving box, we establish the galactocentric coordinates for each galaxy through a two-step process. First, we use the "shrinking spheres" method (C. Power et al. 2003) to determine the center position of each galaxy. We rotate the system to align the total angular momentum of the young stars (age $\leqslant$1 Gyr) along the Z-direction, which orients the Galactic disk in the X–Y plane for each simulation.[8]

We establish the solar circle with a fixed cylindrical radius of $R_\odot = 8.1 \pm 0.6$ kpc (Gravity Collaboration et al. 2018). The rotation curves of these simulations are roughly flat at 8.1 kpc, with values close to 220 ± 20 km s^{-1}, which roughly match that of the MW. Our choice is strictly motivated from the measured solar position; in Section 3.2.1, we discuss our results for the DM density as a function of changing cylindrical radius from the center of each halo and show that the DM densities at $R_\odot = 8.1 \pm 0.6$ kpc are consistent with the MW values within 1σ (see Table 1). Although one could scale the cylindrical radius of each halo based on quantities like the exponential scale length of the Galactic disk or the stellar half-mass radius, the galaxies in this paper are within a factor of 2 in stellar mass (see Table 1). Thus, scaling to a specific scale radius is less critical compared to cases where galaxies have widely different masses. The decision to scale depends on the properties being probed and whether there is a valid reason to expect them to scale with the scale radius at a fixed mass. For example, M. A. Bellardini et al. (2021) found that measuring FIRE-2 galaxies in physical units rather than scaling to a specific radius resulted in less scatter and more self-similarity in their analysis of metallicity radial gradients. Since our results depend on the density at a fixed radius, which does not necessarily scale with the scale radius at a fixed mass, the meaningful "scaling" in this context is to match the local densities rather than adjusting based on a scale radius. We find that using a fixed radius from the center of each halo offers a more consistent and reliable comparison for our analysis.

We select a cylindrical region with a fixed Galactocentric cylindrical radius of $R_\odot = 8.1 \pm 0.6$ kpc and a height of $|Z| \leqslant 5$ kpc, centered around the solar circle. This cylindrical region is then divided into small bins of 50 kpc in the X- and Y-directions, covering $|Z| \leqslant 5$ kpc.[9] Within each of these bins, we independently compute the surface density ($\Sigma_{X,Y}$) for baryons

[8] We also tested other methods to establish the disk plane, such as measuring the spatial midplane, and found that our results remain consistent regardless of the method used.

[9] This value is $\geqslant$10 times larger than the star and gas softening parameters used in the simulations and about 2 times greater than the DM softening.

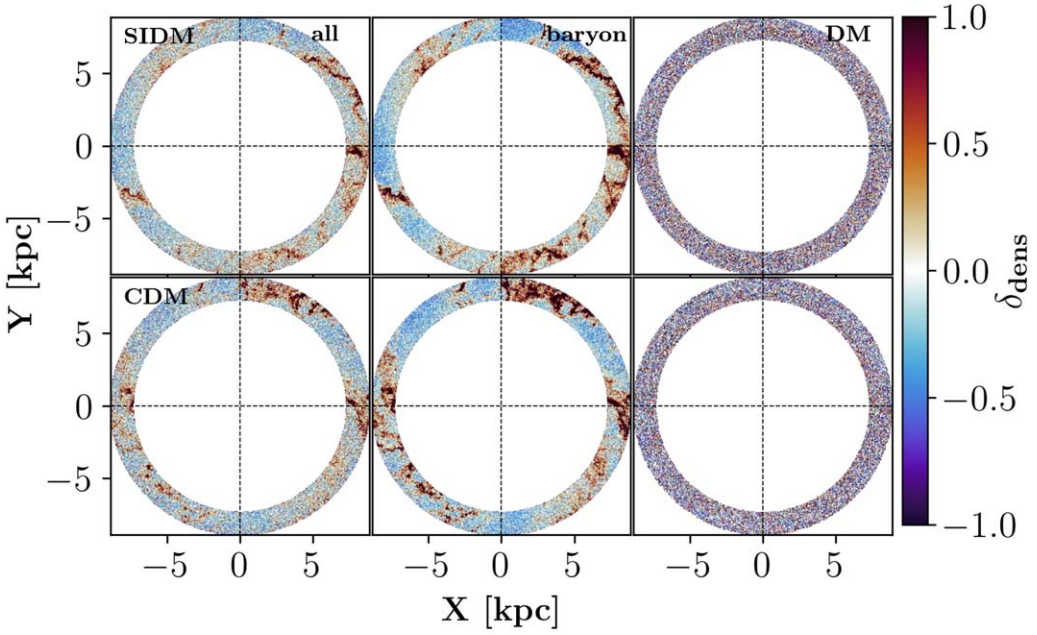

Figure 1. Relative variation in surface density ($\delta_{\rm dens}$) in the X–Y plane around the solar neighborhood within $R_\odot = 8.1 \pm 0.6$ kpc and $|Z| < 5$ kpc for the m12f SIDM (top) and CDM (bottom) halos computed for particle species (all, left; baryons, middle; DM, right). Most variations with overdensities (red) and underdensities (blue) are in the baryonic component, while DM densities are relatively uniform and smooth.

(stars and gas), for DM, and for all (baryons and DM) the species combined together. Following this, we introduce a metric, $\delta_{\rm dens}$, to quantify the relative surface density variation,

$$\delta_{\rm dens} = \frac{\Sigma_{X,Y} - \overline{\Sigma_R}}{\overline{\Sigma_R}}, \quad (1)$$

where $\overline{\Sigma_R}$ is the median surface density at $R = (X^2 + Y^2)^{1/2}$.

Figure 1 illustrates the relative surface density variation ($\delta_{\rm dens}$) for the m12f SIDM (top panel) and CDM (bottom panel) halos at the present day, categorized by species: all (left), baryons (middle), and DM (right). Major density variations are predominantly within the baryonic component, where overdense regions (red) can exhibit densities approximately twice as high ($\delta_{\rm dens} \sim 1$). Conversely, the DM component showcases a uniform distribution, characterized by $|\delta_{\rm dens}| < 0.05$. This uniformity in DM serves to counterbalance the fluctuations observed in baryonic matter. However, when considering all species combined, notable relative density variations persist within the solar neighborhood. Similar patterns are observed in the m12i and m12m simulations. Notably, no discernible systematic trend in densities is observed between the CDM and SIDM models. Furthermore, the majority of the high-density regions exhibit elevated gas density and are actively forming new stars. We note that $\delta_{\rm dens}$ is roughly independent on the choice of Z range.

Next, we categorize the bins into three density regions—low, medium, and high—based on their surface density in quartile ranges of $\leqslant$25th percentile, 25th–75th percentile, and $\geqslant$75th percentile, respectively. The three density regimes effectively provide upper and lower limits on the Galactic acceleration profiles. Table 1 summarizes the galaxy-wide properties along with average variations in the low-, medium-, and high-density regions around the solar circle for all of the simulations.[10] While the median baryonic volume density in the solar circle across all halos is generally much lower (5σ–8σ) compared to the MW, the total surface density across the halos is relatively close to that of the MW (within 2σ–3σ), except for m12i CDM, which is about 6σ away. Also, F. McCluskey et al. (2024) showed that the MW forms an unusually dynamically cold disk, which could explain the higher average density, contrasting with other observed galaxies of similar mass ($\sim 10^{12}\ M_\odot$) through analysis of the Latte disks. Additionally, our estimates for the MW are solely based on the local volume around the solar neighborhood. In terms of matching local properties, the m12m SIDM halo is the most similar to the MW, exhibiting comparable thin and thick disks and cold gas scale heights. We observe that both the total volume and surface density between regions within the same halo can vary by a factor of 2. For example, in the low-, medium-, and high-density regions, the volume density[11] for m12m SIDM is approximately $(36, 50, 79) \times 10^{-3}\ M_\odot\ {\rm pc}^{-3}$. Only ~6% of our selected bins exhibit total volume densities within 1σ of the MW value of $99 \pm 9.5 \times 10^{-3}\ M_\odot\ {\rm pc}^{-3}$, and 10% of the bins have total volume density values higher than the MW. The majority of the variations arise from the baryonic component (stars and gas), and the DM component is evenly distributed azimuthally (lower errors in Table 1; see Figure 1).

Comparing DM models, the SIDM halos exhibit both higher stellar and DM volume and surface densities in the solar neighborhood than their CDM counterparts. This is primarily due to SIDM particles' capacity to exchange energy and momentum in addition to gravity, making them more responsive and sensitive to the baryonic potential (O. D. Elbert et al. 2018; O. Sameie et al. 2018; G. Despali et al. 2019; V. H. Robles et al. 2019; I. M. E. Santos-Santos et al. 2020). The higher DM density facilitates the entrapment of additional gas, forming new stars and establishing a feedback loop, where DM particles can respond faster to the rising stellar density (G. Despali et al. 2019; O. Sameie et al. 2021). While at about

[10] Varying $|Z|$ ranges to match the MW estimates.

[11] For $|Z| \leqslant 0.2$ kpc to match the volume density calculation in the MW.

Table 2
Best-fit Potential Model and Oblateness/Shape Parameters

Galaxy	Physics	$M_{\rm MN}$ ($10^{10}\,M_\odot$)	a (kpc)	b (kpc)	$\log_{10}(-\gamma_{\rm MN}/{\rm Gyr}^{-2})$	$\log_{10}(\alpha_1/{\rm Gyr}^{-2})$	$\log_{10}(-\gamma_{\rm LO}/{\rm Gyr}^{-2})$	$\frac{c}{a}\big\rvert_{R_\odot}$
MW[a]	?	10	6.5	0.26	3.94	3.54 ± 0.16	3.3 ± 0.9	…
m12i	CDM	1.95 ± 0.04	3.91 ± 0.31	0.80 ± 0.12	2.83 ± 0.02	3.00 ± 0.00	2.87 ± 0.01	0.46
	SIDM	3.11 ± 0.07	3.17 ± 0.34	0.85 ± 0.23	3.01 ± 0.03	3.14 ± 0.01	2.99 ± 0.01	0.43
m12f	CDM	3.54 ± 0.13	3.30 ± 0.26	0.82 ± 0.33	3.08 ± 0.05	3.17 ± 0.02	3.15 ± 0.00	0.40
	SIDM	4.20 ± 0.05	3.50 ± 0.18	0.79 ± 0.05	3.17 ± 0.02	3.20 ± 0.00	3.16 ± 0.01	0.38
m12m	CDM	3.49 ± 0.24	6.31 ± 0.44	0.78 ± 0.04	2.97 ± 0.04	3.17 ± 0.01	2.92 ± 0.00	0.30
	SIDM	5.30 ± 0.09	6.81 ± 0.20	0.78 ± 0.04	3.11 ± 0.05	3.28 ± 0.01	2.95 ± 0.01	0.27

Notes. MN profile parameters for the stellar disk for stars within 3 kpc $\leqslant R \leqslant$ 15 kpc and $|Z| \leqslant 1.1$ kpc. LO potential profile parameters near the solar circle, $R_\odot = 8.1$ kpc for stars within $|Z| \leqslant 1.1$ kpc, for the simulated galaxies with different DM models. $\frac{c}{a}|_{R_\odot}$ is the minimum-to-major axis ratio computed using an ellipsoid fit to all matter particles at $R_\odot$.
[a] Values from S. Chakrabarti et al. (2021) and T. Donlon et al. (2024).

8.1 kpc from the Galactic center, we anticipate only about one DM scattering event per particle per Hubble time, these rates are higher in the inner regions of the galaxy (D. Vargya et al. 2022), which leads to more pronounced differences in DM density between CDM and SIDM in the inner regions (see Figure 5 in Section 3.2.1). Consequently, SIDM halos exhibit higher density in DM and stellar distribution within the baryon-dominated potential, resulting in increased oblateness in the inner regions and around the solar circle.

In Section 3.2.1 (see Figure 5), we show the azimuthally average DM density in different 2D cylindrical radii (between 4 and 12 kpc), showing that the trend of denser SIDM holds across a variety of radii. The differences between the CDM and SIDM are more pronounced in the inner regions, and considering that the MW has a thinner disk compared to the simulated galaxies, the expected effect of SIDM versus CDM as a function of vertical distance from the midplane (Z) in the MW should be even more significant.

2.2. Comparison with Local Potential Models

Ideally, one would integrate the acceleration field (from, e.g., pulsar timing or other acceleration measurements) to infer the potential directly. However, in practice, the scarcity of data points (e.g., 20 pulsars within 2 kpc of the Sun; T. Donlon et al. 2024) currently limits our ability to perform such integration. Consequently, in the MW, observers use static parameterization models to fit the available data accurately. Here, we present our simulations with similar parameters through potential model fitting on stars in order for a direct comparison. We consider two axisymmetric potentials previously used in S. Chakrabarti et al. (2021). Specifically, a low-order (LO) expansion $\alpha\gamma$ potential (Equation (2); S. Chakrabarti et al. 2021) near the position of the Sun (i.e., the adopted solar circle in our case) and a single Miyamoto–Nagai (MN) potential (Equation (3)) for the galactic disk.

The LO potential profile is defined as

$$\Phi(R, Z) = V_{\rm LSR}^2 \log(R/R_\odot) + \log(R/R_\odot)\gamma_{\rm LO} Z^2 + \frac{1}{2}\alpha_1 Z^2, \tag{2}$$

where $V_{\rm LSR}$ is the local standard of rest velocity, $\gamma_{\rm LO}$ determines the shape of the potential affecting the vertical accelerations, and α_1 represents the squared angular frequency of oscillations in the vertical density profile. A higher value of $\log -\gamma_{\rm LO}$ indicates a flatter potential profile in the solar neighborhood.

For stars located within $R_\odot = 8.1 \pm 0.6$ kpc and at heights $|Z| \leqslant 1.1$ kpc, localized around the midplane, we fit the LO potential profile parameters $V_{\rm LSR}$, $\gamma_{\rm LO}$, and α_1 using linear regressions on the potential values stored as a property for the particles in the simulation. To estimate the uncertainties on these parameters, we employ a Markov Chain Monte Carlo (MCMC) bootstrap approach, using 1000 samples. This involves repeatedly resampling the data with replacement and fitting the model to each resampled data set.

To model the gravitational effect of the simulated galactic disk for stars within 3 kpc $\leqslant R \leqslant$ 15 kpc and at heights $|Z| \leqslant 1.1$ kpc, we use a single MN profile for the limited vertical range around the midplane, given by

$$\Phi_{\rm MN}(R, Z) = -\frac{GM_{\rm MN}}{\sqrt{R^2 + (a + \sqrt{Z^2 + b^2})^2}}. \tag{3}$$

We fit the 2D density of the simulation with the density functional form of the MN profile using the scale mass ($M_{\rm MN}$), scale radius (a), and scale height (b) for the galactic disk. The fitting is performed using a least-squares optimization method, specifically the Nelder–Mead method (J. C. Lagarias et al. 1998), to find the best-fit parameters and estimate the uncertainties on these parameters using an MCMC bootstrap with 1000 samples. A. Arora et al. (2022) showed that such analytic potential models can reconstruct the rotation curve of the FIRE simulated galaxies to about $\pm 2\%$ accuracy in the disk region.

The oblateness parameter for the MN disk is computed by expanding Equation (3) to first order in R and second order in Z around $(R_\odot, 0)$:

$$\gamma_{\rm MN} = -\frac{GM_{\rm MN}}{b}\frac{a + b}{(R_\odot^2 + (a + b)^2)^{5/2}}\frac{3R_\odot^2}{2}. \tag{4}$$

Table 2 shows the best-fit parameters and oblateness (γ) obtained for the simulations using the LO and MN potentials along with the best-fit parameters for the MW from T. Donlon et al. (2024). The scale radius (a) and scale height (b) from the MN profile fits for all three halos are within 1σ of each other

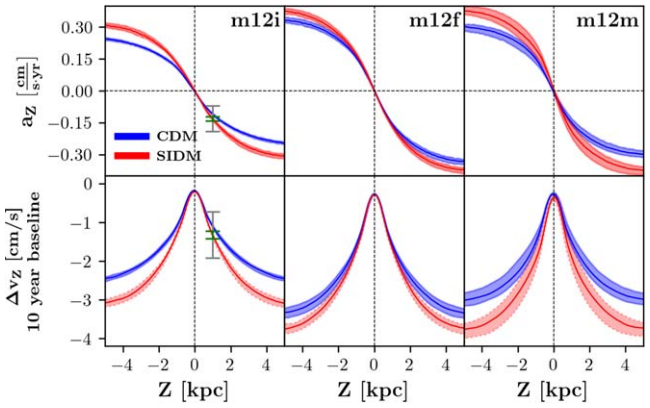

Figure 2. Vertical acceleration (top row) and change in the vertical velocity over a 10 yr baseline (bottom row) as a function of vertical height Z from the solar circle for CDM (blue) and SIDM (red) models in the three simulations (columns). The corresponding shaded regions show the upper and lower limits on the profiles, as computed from high- and low-density bins, respectively. The error bars in the first column show the current (with a 10 yr baseline) measurement uncertainties for pulsar accelerations up to $Z = \pm 1$ kpc (gray) and expected uncertainties with a 20 yr baseline (green) from T. Donlon et al. (2024) by scaling pulsar timing precision by a power of 5/3 (D. R. Lorimer & M. Kramer 2004) centered on the m12i SIDM value at $Z = 1$ kpc for reference. It is evident that both the vertical acceleration profile and the change in vertical velocity have consistently larger values in the SIDM simulations compared to their CDM counterparts.

when comparing the CDM and SIDM models. It is noteworthy that the γ values derived from the LO potential ($\gamma_{\rm LO}$) and the MN disk ($\gamma_{\rm MN}$) are similar in all simulations, except for the m12m SIDM case. This suggests that the shape of the local potential at the solar circle is primary influenced by the stellar disk.

The values obtained in the simulations are within 0.5σ of the MW best-fit parameters from T. Donlon et al. (2024). Our simulated SIDM halos match the observed MW values better than the CDM counterparts, particularly with regard to the shape and oblateness of DM halos. Specifically, the SIDM halos at the solar circle demonstrate lower minor-to-major axis ratios (by 0.02–0.03); in other words, they are more oblate than the CDM halos. This happens because SIDM magnifies the variations in the star formation rate that enhance the concentration of both baryons and DM (see Table 1).

3. Vertical Acceleration Profiles

We calculate the vertical accelerations above and below the Galactic midplane using a binned method ($\Delta Z = 0.05$ kpc) to present smooth trends as a function of vertical distance (Z) from the midplane. We slice the low-, medium-, and high-density regions as defined in Section 2.1 into 50 kpc vertical distance Z bins.[12] Next, we average the gravitational accelerations computed for stars and DM particles in each region within each Z bin. With this approach, we obtain a smooth and accurate representation of the median acceleration profile; the high-density bin provides an upper limit, and the low-density bin provides a lower limit for each profile.

Figure 2 plots the vertical acceleration a_Z (top row) and the change in the vertical velocity over a 10 yr baseline ($\Delta v_Z \equiv a_Z \Delta t$; bottom row) at the present day for m12i (left column), m12f (middle column), and m12m (right column) in CDM (blue) and SIDM (red) model. The shaded regions represent the upper and lower limits on the profiles derived from the high- and low-density regions, respectively. SIDM halos have consistently larger magnitudes of acceleration than CDM, thanks to their higher surface densities, especially at larger distances from the midplane. The error bars in the first column represent current average measurement uncertainties for pulsar accelerations up to $Z = \pm 1$ kpc (gray error bars) centered on the m12i SIDM value at $Z = 1$ kpc for reference, derived from pulsar timing data over a 10 yr baseline, and the expected uncertainties for a 20 yr baseline (green error bars) as reported in T. Donlon et al. (2024) scaling pulsar timing precision by a power of 5/3 (D. R. Lorimer & M. Kramer 2004). The estimated future uncertainties are expected to distinguish between the profile differences noted between the CDM and SIDM models. We note that the degree of difference in Δv_Z between the SIDM and CDM profiles varies with the simulation, with the smallest difference observed for m12f (one with a massive merger about 3 Gyr before the present day) and the largest difference for m12m (no mergers in the last 10 Gyr). This observation suggests that mergers may have a role in removing or mitigating differences between SIDM and CDM profiles. We discuss this more in Section 3.2.

3.1. Median Vertical Acceleration Gradient

Figure 3 depicts the vertical acceleration gradient ($\frac{da_Z}{dZ}$; left) and the asymmetric difference around the midplane (right) as a function of vertical height Z for simulations (color-coded) in CDM (solid line) and SIDM (dotted line) models. The gradients are computed using a total-variation regularization differentiation algorithm that avoids the noise amplification in finite-difference methods for noisy data (R. Chartrand 2011). The asymmetric difference is given by

$$\left|\Delta \frac{da_Z}{dZ}\right| \equiv \left| \frac{da_Z}{dZ}\right]_{+Z} - \frac{da_Z}{dZ}\Big]_{-Z} \Bigg|. \quad (5)$$

The gray shaded region indicates the current measurement uncertainty in $\frac{da_Z}{dZ}$ from T. Donlon et al. (2024), while the green shaded region represents the anticipated measurement uncertainty with a 20 yr baseline (D. R. Lorimer & M. Kramer 2004). Note that the majority of the azimuthal variation stems from the *observable* baryonic component, and the azimuthal distribution of DM is effectively constant in these simulations. In fact, variations arising from the baryonic component can be mitigated with precise measurements; as such, we only show the median profiles for $\frac{da_Z}{dZ}$ in Figures 3, 4, and 5.

The $\frac{da_Z}{dZ}$ at the midplane ($Z = 0$ kpc) in our simulations closely aligns with the MW's best-fit value of -3200 ± 2560 Gyr^{-2} (T. Donlon et al. 2024), albeit within 1σ error of the MW measurement. Discrepancies primarily arise from lower median total matter density in the solar neighborhood in the simulations relative to the measured MW values that are locally measured. S. Chakrabarti et al. (2021) reported a value of -4900^{+1600}_{-2700} Gyr^{-2} using data from 14 binary pulsars distributed over $\sim$1 kpc from the Sun, which is comparable to the more updated value given in T. Donlon et al. (2024). This value corresponds to the square of the frequency of low-amplitude vertical oscillations (denoted α_1 in S. Chakrabarti et al. 2021) and is used to determine the midplane density, or

[12] This value is $\geqslant$10 times greater than the softening parameters used in the simulations.

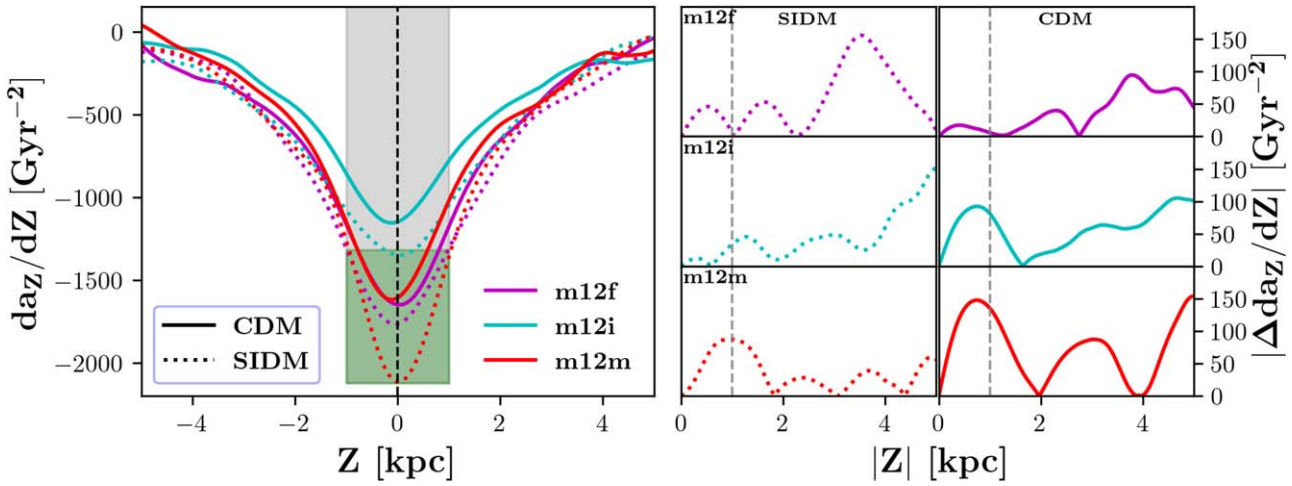

Figure 3. Vertical acceleration gradient ($\frac{da_Z}{dZ}(Z)$; left) and the asymmetric difference between $+Z$ and $-Z$ (right) with respect to vertical height Z for CDM (solid) and SIDM (dotted) halos. SIDM halos have consistently steeper profiles compared to the CDM halos. Notable asymmetries are observed in m12f and m12i for $Z \geqslant 1$ kpc (dashed line in second panel). The MW's measured $\frac{da_Z}{dZ}$ at the midplane is approximately -3200 Gyr^{-2}. Gray shading represents the current measurement uncertainty for pulsar studies in $\frac{da_Z}{dZ}$ (S. Chakrabarti et al. 2021; T. Donlon et al. 2024), and the green region indicates the expected precision increase, scaling pulsar timing precision by a power of 5/3 over a 20 yr baseline (D. R. Lorimer & M. Kramer 2004). Both the shaded regions are scaled to match the minimum value in m12m SIDM. Figure 5 in Section 3.2.1 plots the da_Z/dZ ($Z = 0$) at the midplane ($Z = 0$) as a function of 2D cylindrical radius. SIDM halos show consistently larger values of $\frac{da_Z}{dZ}(Z = 0)$ across a range of radii. The differences between CDM and SIDM are more pronounced closer to the galactic center.

the Oort limit. This gives a value of the Oort limit of $0.08^{0.05}_{-0.02}\, M_\odot$ pc^{-3}, which is close to but lower than kinematic estimates. Due to the limitation of data available at that time, the analysis in S. Chakrabarti et al. (2021) could not constrain global properties, like the mass. T. Donlon et al. (2024) find a value for the Oort limit of $0.062 \pm 0.017\, M_\odot$ pc^{-3}, which is lower still relative to kinematic estimates. Using simplified density profiles, T. Donlon et al. (2024) estimate the galaxy mass within the solar circle to be nearly twice as high as the currently accepted value from J. Bland-Hawthorn & O. Gerhard (2016). MW measurements may, however, be impacted by high uncertainties currently in binary pulsar data. These measurements will continue to improve as more pulsar timing data become available.

Notably, the depth of $\frac{da_Z}{dZ}(Z)$ as a function of vertical distance from the midplane varies significantly across simulations, with SIDM simulations consistently displaying deeper valleys by 10%–30% within 1 kpc of the midplane. The most substantial gradient and the most pronounced difference between SIDM and CDM profiles are observed in m12m because it is the most massive disk (interestingly, it also has the lowest Toomre Q value). In contrast, m12i CDM displays the shallowest valley close to the midplane, aligning with the volume densities of their respective systems. Interestingly, m12f, which experienced a recent merger, shows the least pronounced difference between CDM and SIDM profiles, while m12m, which had the earliest merger, exhibits the most significant difference between the DM profiles close to the midplane. In the outskirts ($|Z| \geqslant 2$ kpc), the difference between profiles is smaller. This observation suggests that the presence of recent major mergers such as Sag dSph and the LMC in a galaxy might mitigate the distinctive signatures of DM models on the vertical acceleration gradient profile, particularly close to the midplane. This could be due to multiple factors, such as an epoch of increased star formation triggered by the influx of gas from the merging satellites (P. Di Matteo et al. 2007; P. F. Hopkins et al. 2010; W. Pearson et al. 2019) and/or heating of the galactic center due to the energy exchange with the merging satellite (e.g., J. E. Barnes & L. Hernquist 1992).

Given the uncertainties regarding the exact location of the solar circle within our simulation, Section 3.2.1, Figure 5 shows $\frac{da_Z}{dZ}$ as a function of 2D cylindrical radius spanning a range of 4–12 kpc. SIDM halos have consistently higher values of $\frac{da_Z}{dZ}(Z = 0)$ across all radii. The difference between the SIDM and CDM models is most pronounced near the galactic center. Notably, while m12m exhibits the most significant difference, m12f displays relatively minor disparities, aligning with the trends observed in Figure 3. These highlight the consistency of our results across a broad range of radii.

We also note a significant asymmetry around the midplane in $\frac{da_Z}{dZ}$ (right panels in Figure 3) that is particularly pronounced for m12f, which underwent recent massive mergers, and also for m12i. In contrast, m12m, which had no recent mergers in the CDM case, exhibits a less pronounced asymmetry. For SIDM simulations, a similar trend is observed between m12f and m12i, with noticeable asymmetries in m12m as well.

These asymmetries are influenced by various factors, including the orbits of merging satellites, which can excite long-standing nodes in the Galactic disk (M. D. Weinberg 1998), leading to higher variation in azimuthal direction. As argued by S. Chakrabarti et al. (2019, 2020), recent mergers leave a discernible imprint on the vertical acceleration profiles persisting long after the complete tidal stripping of satellites. These signatures become more pronounced at greater distances from the midplane, highlighting the enduring impact of recent merger events. We observe large vertical asymmetries, especially in the gas disk in the outer part of the MW (E. S. Levine et al. 2006), that may arise from an interaction with a massive DM subhalo (S. Chakrabarti & L. Blitz 2009). The global asymmetries in the baryonic component may allow us, together with the observed asymmetry in the total acceleration field, to more comprehensively model past interactions with dwarf galaxies.

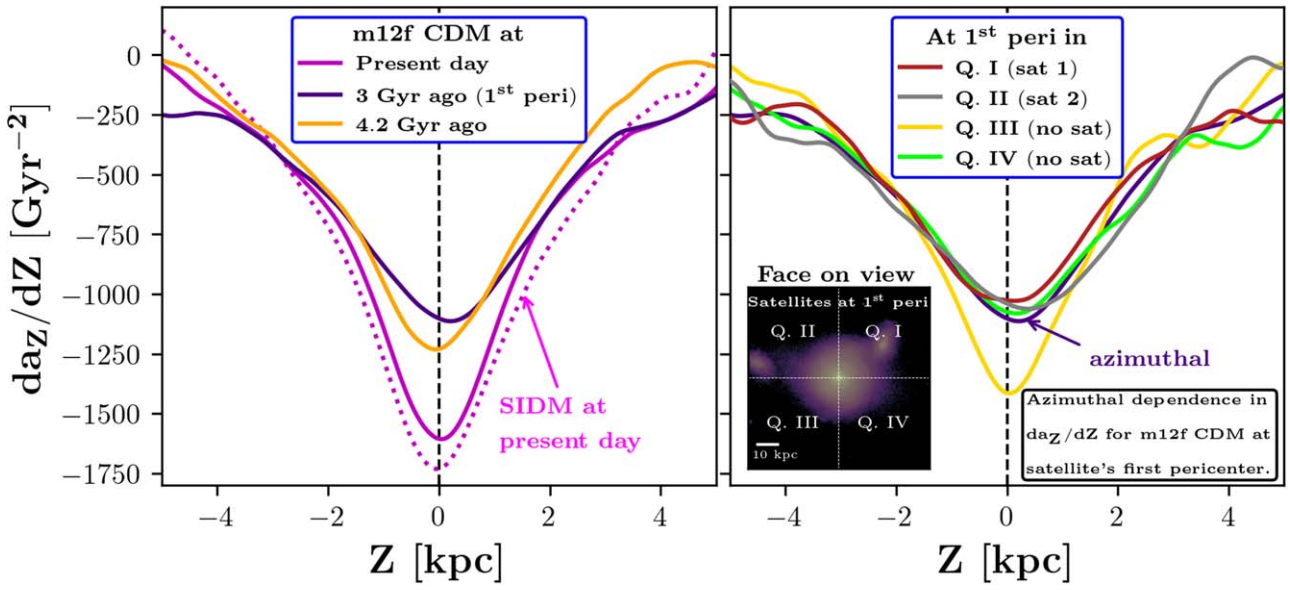

Figure 4. Left: azimuthally averaged vertical acceleration gradient ($\frac{da_Z}{dZ}$) as a function of vertical height Z for the m12f CDM halo at different epochs: at the present day (magenta color) for CDM (solid) and SIDM (dotted), at the time of the satellite's first pericentric passage (3 Gyr before the present day; indigo color), and 4.2 Gyr before the present day (orange color). Before the merger event, the profile is symmetric across the midplane ($Z = 0$), but it becomes highly asymmetric during the merger and retains some asymmetry until the present day. Right: the vertical acceleration gradient ($\frac{da_Z}{dZ}$) computed in different quadrants (marked in insets in the bottom left corner) for the m12f CDM halo at the time of the first pericentric passage. Q. I and II, which contain two satellites close to pericenter, exhibit the most asymmetry across the midplane. In contrast, Q. III and IV, which have no satellites, display relatively symmetric profiles. The inset in the bottom left plots the disk plane for the m12f CDM at first pericenter and marks the relevant quadrants.

3.2. Temporal and Spatial Variation in the Vertical Acceleration Gradient

In previous sections, we observed a consistent trend: azimuthally averaged vertical acceleration gradient profiles in SIDM simulations were systematically steeper, typically by 10%–30%, compared to their CDM counterparts. However, it remains to be seen whether the temporal and azimuthal variations expected in $\frac{da_Z}{dZ}(Z)$ are similar in level and scale to the DM model-dependent differences, because if this is true, it could imply that the variations we see in the simulations might not be due to actual differences in DM properties but are actually transient effects due to mergers. In this section, we examine the spatial and temporal variations in $\frac{da_Z}{dZ}(Z)$à using the m12f CDM simulation as an example. This simulation experienced a major merger with two satellites with their first pericentric passage approximately 3 Gyr ago with a total mass ratio of 15 and 18, when each satellite was at a pericentric distance of about 25 kpc.[13]

The left panel of Figure 4 illustrates the azimuthally averaged $\frac{da_Z}{dZ}(Z)$ profiles at various epochs: the present day (magenta) for both CDM (solid) and SIDM (dotted), during the first pericentric passage (3 Gyr before the present day; indigo), and 4.2 Gyr before the present day (orange). These profiles display significant variations (10%–30%) in depth, influenced by the average total matter density. Approximately 1 Gyr before the pericentric passage, the profile is steeper due to enhanced star formation in the region around the solar circle and symmetric around the midplane. At the first pericentric passage, the profile is shallower and highly asymmetric. By the present day, the increasing baryon density has substantially steepened the acceleration profile, with the asymmetry persisting to some extent. These temporal variations in profile depth are comparable to the highest-order variations seen in m12m CDM and SIDM profiles in Figure 3 and higher than the variations observed in the the m12f CDM and SIDM profiles.

The right panel of Figure 4 depicts $\frac{da_Z}{dZ}(Z)$ computed in four azimuthal quadrants (marked in insets on the bottom left) during the first pericentric passage in m12f CDM. All quadrants exhibit consistent profile depths within a 10% range except for Q. III, which shows increased depth due to high-density gas prompting new star formation. The variation at large $|Z|$ stems from limited particle data away from the midplane leading to noisy gradients. Quadrants containing the two satellites (Q. I and II) display more significant asymmetry across the midplane, while the quadrants without any satellites (Q. III and IV) have relatively symmetric profiles, highlighting the impact of satellite orbits on gradient asymmetry.

3.2.1. Radial Variation in the Local DM Density

Figure 5 plots the azimuthally averaged DM density[14] ($\rho_{\rm DM}$) calculated within a vertical range of $|Z| \leqslant 0.2$ kpc (left) and the vertical acceleration gradient ($\frac{da_Z}{dZ}(Z = 0)$) at the midplane ($Z = 0$ kpc) as a function of 2D cylindrical radius ($R_{\rm cylindrical}$) for the three simulations (color-coded) in both CDM (circles) and SIDM (plus signs) models. In the inner regions of the galaxies, SIDM models, influenced by the baryonic component, exhibit systematically higher DM density and steeper gradients at the midplane compared to their CDM counterparts for all radii. These differences decrease further away from the center. These pronounced differences are consistent with the higher scattering rates of DM particles close to the center (D. Vargya et al. 2022).

[13] Defined as the ratio of the total mass of the main halo divided by the total mass of the satellite at the moment of first pericentric passage.

[14] Similar to Table 1.

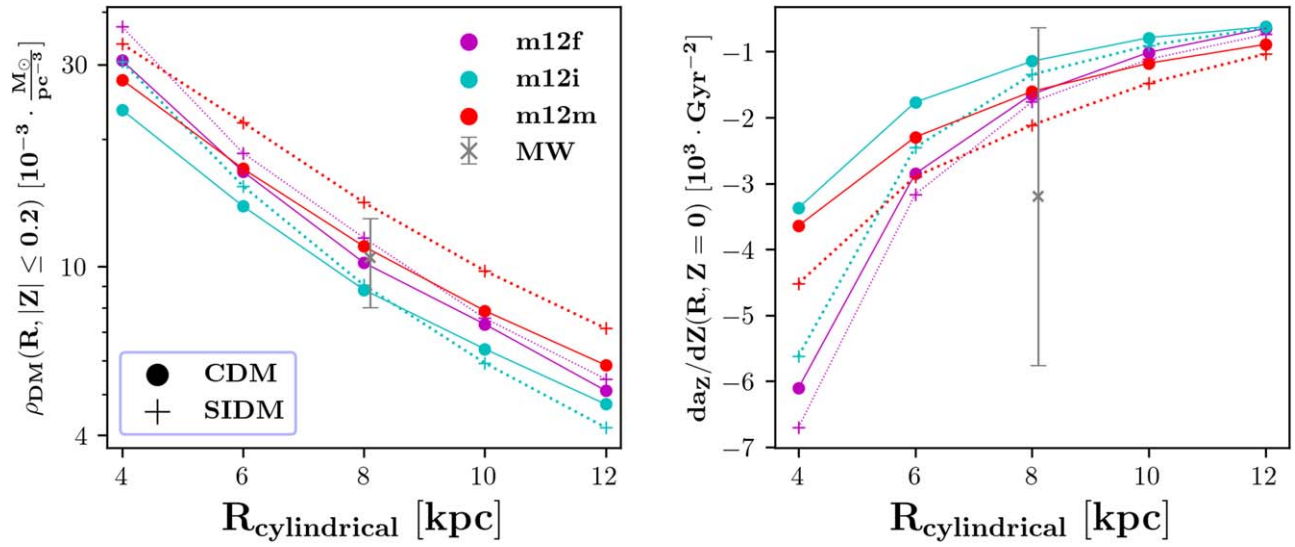

Figure 5. Left: azimuthally averaged DM density (ρ_{DM}) within a vertical range of $|Z| \leqslant 0.2$ kpc as a function of 2D cylindrical radius ($R_{cylindrical}$) for m12f (magenta), m12i (cyan), and m12m (red) for CDM (solid circles) and SIDM (plus signs) at the present day. In general, SIDM halos have a higher DM density closer to the galactic center. Notably, m12m SIDM maintains a consistently higher density compared to the CDM, whereas the m12i halo, with the lowest stellar mass (see Table 1), shows a transition where SIDM becomes less dense (puffier) compared to CDM close to 8 kpc. Right: vertical acceleration gradient ($\frac{da_Z}{dZ}(Z = 0)$) at the midplane ($Z = 0$ kpc) as a function of cylindrical radius ($R_{cylindrical}$) for all the halos as in the left panel. The trends in $\frac{da_Z}{dZ}(Z = 0)$ are similar to those observed in DM density, with SIDM consistently exhibiting steeper gradients compared to CDM. The differences between SIDM and CDM are more pronounced closer to the center. Additionally, the current MW DM density (J. Bland-Hawthorn & O. Gerhard 2016) and $\frac{da_Z}{dZ}(Z = 0)$ (T. Donlon et al. 2024) are shown with gray crosses with error bars.

In m12m, SIDM maintains more pronounced differences between densities and $\frac{da_Z}{dZ}(Z = 0)$ even at larger $R_{cylindrical}$, with no sign of convergence between CDM and SIDM up to 12 kpc. Conversely, in m12i, beyond 8 kpc, the SIDM profile becomes less dense than the CDM profile. This "puffier" profile is due to the absence of a strong baryonic potential in the outskirts, allowing DM particles to self-interact and form less dense, rounder profiles. Additionally, there are minor differences in the $\frac{da_Z}{dZ}(Z = 0)$ at larger $R_{cylindrical}$. Furthermore, m12f exhibits the least variation between CDM and SIDM at all radii in both density and $\frac{da_Z}{dZ}(Z = 0)$. However, $\frac{da_Z}{dZ}(Z = 0)$ remains systematically steeper in the SIDM model.

The galactic disks in these simulated halos are thicker compared to the MW's disk (A. Wetzel et al. 2023; F. McCluskey et al. 2024). This implies that the effects of SIDM versus CDM could be even more pronounced in a thinner disk like that of the MW.

4. Discussion and Conclusions

Direct measurement of Galactic accelerations presents a promising avenue for testing DM, bypassing the need to solve the "inverse problem" (J. Binney & S. Tremaine 2011) inherent in traditional methods of inferring the mass distribution within galaxies from observed motions. By comparing observed acceleration profiles with predictions from simulations with different DM models, we can assess the compatibility of these models with observational data. However, testing SIDM in particular with this strategy offers some challenges due to the ability of SIDM to respond efficiently to changes in the baryon distribution. Galaxy formation can alter even the shape and density profile of a CDM halo; in SIDM, which can more easily alter its energy and angular momentum through interactions, the expectation is that the halo's shape and profile are more tightly correlated with the disk properties (O. Sameie et al. 2021; D. Vargya et al. 2022). However, this response from the SIDM component in the galaxy subsequently affects the baryonic disk, since the deepened DM potential increases the gas density and boosts star formation. Thus, the long-term coevolution of the SIDM and baryons leads to a slightly higher stellar mass, a slightly more dense DM halo in the disk plane, and slightly higher star formation rates than in CDM. These differences are evident in our Table 1 and Figure 5 and are the means by which SIDM solves the so-called "diversity problem."

At the solar circle, the distribution and properties of baryonic matter play a role equal to or larger than DM's in creating the observed Galactic acceleration profiles (see Figure 4). The steeper vertical acceleration gradients in SIDM relative to the same halo in CDM (Figure 3), which are calculated at the solar circle, thus reflect the response of both species to the change in the DM model. However, the variation in the acceleration profile among CDM galaxies, which is simply due to their different star formation and assembly histories, spans nearly as large a range. Thus, observations of the density distribution in the MW alone are unlikely to distinguish CDM from SIDM. However, a large sample of measurements of the disk-plane density of galaxies could potentially show a signal, since in SIDM, one would expect the mean density in such a sample to be statistically higher than expected from CDM. The trend of density with radius in such a sample may also help distinguish the two theories, since the differences in density between CDM and SIDM become more pronounced at smaller radii (where one expects more frequent self-interactions). At the solar circle (8.1 kpc), with a cross section of 1 cm^2 g^{-1}, we expect about one scattering event per Hubble time ($\sim$10 Gyr) per DM particle in our simulations, with much higher scattering rates in the inner regions of the galaxy (D. Vargya et al. 2022).

Measuring Galactic accelerations may help to illuminate the merger history of the MW, since mergers induce asymmetries in the acceleration profile (S. Chakrabarti et al. 2021; see Figures 3 and 4). This highlights the need for flexible

disequilibrium models to fully utilize acceleration data (T. Donlon et al. 2024), given that merger-induced variations often exceed the differences induced by changing the DM model. Additionally, we only explored the Galactic acceleration profiles in simulations run with standard Monte Carlo implementation for SIDM (A. H. G. Peter et al. 2013; M. Rocha et al. 2013) using the FIRE-2 prescription for baryons (P. F. Hopkins et al. 2018). In the future, one should explore different simulation suites performed with varied baryon prescriptions (e.g., R. Teyssier 2002; H. Menon et al. 2015; J. W. Wadsley et al. 2017; R. Weinberger et al. 2020) and alternative SIDM implementations (e.g., M. Vogelsberger et al. 2012; A. B. Fry et al. 2015; H. Meskhidze et al. 2022).

Our main conclusions are summarized below.

1. The solar neighborhood in the MW is comparatively denser than the median of the azimuthally averaged solar circle regions in these three FIRE-2 simulations with the CDM and SIDM models (see Section 2.1 and Table 1). Regions with local density similar to the solar neighborhood are relatively limited and make up about 6% of the volume at the solar circle. The higher density in the MW can be attributed to the relatively thin MW disk even compared to other $\sim 10^{12}\ M_{\odot}$ galaxies (F. McCluskey et al. 2024) and/or our placement in a dense region of the Galaxy. It should be noted that we did not explore all of the FIRE-2 MW-mass simulations, so a systematic comparison to better quantify this in relation to the MW remains to be conducted.
2. The shape of the potential and the density in the solar neighborhood are predominantly influenced by the Galactic disk (see Section 2.2). However, SIDM particles showing greater responsiveness to the disk potential leads to higher flattening in the DM shape at the solar circle. This leads to measurable distinctions in the local DM density within the solar neighborhood. SIDM halos consistently demonstrate denser and more oblate potentials, resulting in vertical acceleration gradient profiles that are steeper by 10%–30% compared to CDM (see Section 3.1 and Figure 3). However, the galaxy-to-galaxy variation in density is broader than the difference between SIDM and CDM at $1\ \mathrm{cm}^{-2}\ \mathrm{g}^{-1}$.
3. Recent mergers with total mass equal to or greater than the Sagittarius dwarf or the SMC will induce measurable asymmetries across the midplane in the vertical acceleration gradient profiles (S. Chakrabarti et al. 2019, 2020), which can persist over extended periods to the present day (see Section 3.2 and Figure 4). These asymmetries—influenced by factors such as satellite mass and orbit—can be larger than the systematic difference between SIDM and CDM, which poses challenges for probing the nature of DM in a single galaxy. Nonetheless, these asymmetric profiles are a promising probe of the merging history of a galaxy.

Acknowledgments

A.A. and R.E.S. acknowledge support from the Research Corporation through the Scialog Fellows program on Time Domain Astronomy, from NSF grant AST-2007232, and from NASA grant No. 19-ATP19-0068. R.E.S. is supported in part by a Sloan Fellowship. S.C. acknowledges support from Research Corporation through the Scialog Fellows program on Time Domain Astronomy and from NSF AST 2009828. A.W. received support from NSF via CAREER award AST-2045928 and grant AST-2107772, NASA ATP grant No. 80NSSC20K0513, and HST grant No. GO-16273 from STScI. S.L. acknowledges support from NSF grant AST-2109234 and HST grant No. AR-16624 from STScI. L.N. acknowledges the support of NSF through the CAREER award AST-2337864 and grant AST-2307788 as well as the Sloan Foundation.

This research is part of the Frontera computing project at the Texas Advanced Computing Center (TACC). Frontera is made possible by National Science Foundation award OAC-1818253. Simulations in this project were run using Early Science Allocation 1923870 and analyzed using computing resources supported by the Scientific Computing Core at the Flatiron Institute. This work used additional computational resources of the University of Texas at Austin and TACC, the NASA Advanced Supercomputing (NAS) Division and the NASA Center for Climate Simulation (NCCS), and the Extreme Science and Engineering Discovery Environment (XSEDE), which is supported by National Science Foundation grant No. OCI-1053575.

Software: IPython (F. Perez & B. E. Granger 2007), Matplotlib (J. D. Hunter 2007), Numpy (C. R. Harris et al. 2020), Scipy (P. Virtanen et al. 2020), `halo_analysis` (A. Wetzel & S. Garrison-Kimmel 2020a), `gizmo_analysis` (A. Wetzel & S. Garrison-Kimmel 2020b), CMasher (E. van der Velden 2020).

ORCID iDs

Arpit Arora https://orcid.org/0000-0002-8354-7356
Robyn E. Sanderson https://orcid.org/0000-0003-3939-3297
Sukanya Chakrabarti https://orcid.org/0000-0001-6711-8140
Andrew Wetzel https://orcid.org/0000-0003-0603-8942
Thomas Donlon II https://orcid.org/0000-0002-7746-8993
Danny Horta https://orcid.org/0000-0003-1856-2151
Sarah R. Loebman https://orcid.org/0000-0003-3217-5967
Lina Necib https://orcid.org/0000-0003-2806-1414
Micah Oeur https://orcid.org/0000-0001-5636-3108

References

Arora, A., Sanderson, R. E., Panithanpaisal, N., et al. 2022, ApJ, 939, 2
Barnes, J. E., & Hernquist, L. 1992, ARA&A, 30, 705
Bellardini, M. A., Wetzel, A., Loebman, S. R., et al. 2021, MNRAS, 505, 4586
Belokurov, V., Erkal, D., Evans, N. W., Koposov, S. E., & Deason, A. J. 2018, MNRAS, 478, 611
Besla, G., Kallivayalil, N., Hernquist, L., et al. 2007, ApJ, 668, 949
Binney, J., & Tremaine, S. 2011, Galactic dynamics (2nd ed.; Princeton, NJ: Princeton Univ. Press)
Bland-Hawthorn, J., & Gerhard, O. 2016, ARA&A, 54, 529
Bullock, J. S., & Boylan-Kolchin, M. 2017, ARA&A, 55, 343
Carlson, E. D., Machacek, M. E., & Hall, L. J. 1992, ApJ, 398, 43
Cautun, M., Benitez-Llambay, A., Deason, A. J., et al. 2020, MNRAS, 494, 4291
Chakrabarti, S., & Blitz, L. 2009, MNRAS, 399, L118
Chakrabarti, S., Chang, P., Lam, M. T., Vigeland, S. J., & Quillen, A. C. 2021, ApJL, 907, L26
Chakrabarti, S., Chang, P., Price-Whelan, A. M., et al. 2019, ApJ, 886, 67
Chakrabarti, S., Drlica-Wagner, A., Li, T. S., et al. 2022a, arXiv:2203.06200
Chakrabarti, S., Stevens, D. J., Wright, J., et al. 2022b, ApJL, 928, L17
Chakrabarti, S., Wright, J., Chang, P., et al. 2020, ApJL, 902, L28
Chartrand, R. 2011, Int. Scholarly Res. Not., 2011, 164564
Colin, P., Avila-Reese, V., Valenzuela, O., & Firmani, C. 2002, ApJ, 581, 777
de Boer, T. J. L., Belokurov, V., & Koposov, S. 2015, MNRAS, 451, 3489
de Salas, P. F., & Widmark, A. 2021, RPPh, 84, 104901
Debattista, V. P., Gonzalez, O. A., Sanderson, R. E., et al. 2019, MNRAS, 485, 5073

Despali, G., Sparre, M., Vegetti, S., et al. 2019, MNRAS, 484, 4563
Di Matteo, P., Combes, F., Melchior, A.-L., & Semelin, B. 2007, A&A, 468, 61
Donlon, T., Chakrabarti, S., Widrow, L. M., et al. 2024, PhRvD, 110, 023026
Ebisu, T., Ishiyama, T., & Hayashi, K. 2022, PhRvD, 105, 023016
El-Badry, K., Quataert, E., Wetzel, A., et al. 2018, MNRAS, 473, 1930
Elbert, O. D., Bullock, J. S., Kaplinghat, M., et al. 2018, ApJ, 853, 109
Escala, I., Wetzel, A., Kirby, E. N., et al. 2018, MNRAS, 474, 2194
Evans, N. W., Gyuk, G., Turner, M. S., & Binney, J. 1998, ApJ, 501, L45
Fischer, D. A., Anglada-Escude, G., Arriagada, P., et al. 2016, PASP, 128, 066001
Flores, R. A., & Primack, J. R. 1994, arXiv:astro-ph/9402004
Fry, A. B., Governato, F., Pontzen, A., et al. 2015, MNRAS, 452, 1468
Garavito-Camargo, N., Price-Whelan, A. M., Samuel, J., et al. 2023, arXiv:2311.11359
Gentile, G., Salucci, P., Klein, U., Vergani, D., & Kalberla, P. 2004, MNRAS, 351, 903
Gibbons, S., Belokurov, V., & Evans, N. 2017, MNRAS, 464, 794
Goncharov, B., Reardon, D. J., Shannon, R. M., et al. 2021, MNRAS, 502, 478
Gravity Collaboration, Abuter, R., Amorim, A., et al. 2018, A&A, 615, L15
Guo, R., Liu, C., Mao, S., et al. 2020, MNRAS, 495, 4828
Haines, T., D'Onghia, E., Famaey, B., Laporte, C., & Hernquist, L. 2019, ApJL, 879, L15
Harris, C. R., Millman, K. J., van der Walt, S. J., et al. 2020, Natur, 585, 357
Helmi, A., Babusiaux, C., Koppelman, H. H., et al. 2018, Natur, 563, 85
Hełminiak, K. G., Konacki, M., Maehara, H., et al. 2019, MNRAS, 484, 451
Hopkins, P. F. 2015, MNRAS, 450, 53
Hopkins, P. F., Younger, J. D., Hayward, C. C., Narayanan, D., & Hernquist, L. 2010, MNRAS, 402, 1693
Hopkins, P. F., Wetzel, A., Keres, D., et al. 2018, MNRAS, 480, 800
Hunter, J. D. 2007, CSE, 9, 90
Ibata, R. A., Gilmore, G., & Irwin, M. J. 1994, Natur, 370, 194
Jiang, I.-G., & Binney, J. 2000, MNRAS, 314, 468
Johnston, K. V., Spergel, D. N., & Hernquist, L. 1995, arXiv:astro-ph/9502005
Kahlhoefer, F., Kaplinghat, M., Slatyer, T. R., & Wu, C.-L. 2019, JCAP, 2019, 010
Kallivayalil, N., van der Marel, R. P., Besla, G., Anderson, J., & Alcock, C. 2013, ApJ, 764, 161
Kaplinghat, M., Tulin, S., & Yu, H.-B. 2016, PhRvL, 116, 041302
Keith, M. J., Coles, W., Shannon, R. M., et al. 2013, MNRAS, 429, 2161
Kim, J.-h., Abel, T., Agertz, O., et al. 2014, ApJS, 210, 14
Lagarias, J. C., Reeds, J. A., Wright, M. H., & Wright, P. E. 1998, SIAM Journal on Optimization, 9, 112
Levine, E. S., Blitz, L., & Heiles, C. 2006, ApJ, 643, 881
Loebman, S. R., Ivezic, Ž., Quinn, T. R., et al. 2012, ApJL, 758, L23
Loebman, S. R., Ivezic, Ž., Quinn, T. R., et al. 2014, ApJ, 794, 151
Lorimer, D. R., & Kramer, M. 2004, Handbook of Pulsar Astronomy, Vol. 4 (Cambridge: Cambridge Univ. Press)
Ma, X., Hopkins, P. F., Wetzel, A. R., et al. 2017, MNRAS, 467, 2430
McCluskey, F., Wetzel, A., Loebman, S. R., et al. 2024, MNRAS, 527, 6926
McKee, C. F., Parravano, A., & Hollenbach, D. J. 2015, ApJ, 814, 13
Menon, H., Wesolowski, L., Zheng, G., et al. 2015, ComAC, 2, 1
Meskhidze, H., Mercado, F. J., Sameie, O., et al. 2022, MNRAS, 513, 2600
Monaghan, J. J., & Lattanzio, J. C. 1985, A&A, 149, 135
Moore, B. 1994, Natur, 370, 629
Moore, B., Quinn, T., Governato, F., Stadel, J., & Lake, G. 1999, MNRAS, 310, 1147
Necib, L., Lisanti, M., Garrison-Kimmel, S., et al. 2019, ApJ, 883, 27
Newberg, H. J., Yanny, B., Rockosi, C., et al. 2002, ApJ, 569, 245
Niederste-Ostholt, M., Belokurov, V., Evans, N. W., & Penarrubia, J. 2010, ApJ, 712, 516
Oman, K. A., Navarro, J. F., Fattahi, A., et al. 2015, MNRAS, 452, 3650
Ostriker, E. C., & Binney, J. J. 1989, MNRAS, 237, 785
Ou, X., Eilers, A.-C., Necib, L., & Frebel, A. 2024, MNRAS, 528, 693
Pearson, W., Wang, L., Alpaslan, M., et al. 2019, A&A, 631, A51
Pennucci, T. T. 2019, ApJ, 871, 34
Pepe, F., Cristiani, S., Rebolo, R., et al. 2021, A&A, 645, A96
Perez, F., & Granger, B. E. 2007, CSE, 9, 21
Peter, A. H. G., Rocha, M., Bullock, J. S., & Kaplinghat, M. 2013, MNRAS, 430, 105
Phillips, D. F., Ravi, A., Ebadi, R., & Walsworth, R. L. 2021, PhRvL, 126, 141103
Planck, C., Aghanim, N., Akrami, Y., et al. 2020, A&A, 641, A6
Power, C., Navarro, J. F., Jenkins, A., et al. 2003, MNRAS, 338, 14
Price-Whelan, A. M. 2017, JOSS, 2, 388
Quercellini, C., Amendola, L., & Balbi, A. 2008, MNRAS, 391, 1308
Randall, S. W., Markevitch, M., Clowe, D., Gonzalez, A. H., & Bradac, M. 2008, ApJ, 679, 1173
Robles, V. H., Kelley, T., Bullock, J. S., & Kaplinghat, M. 2019, MNRAS, 490, 2117
Rocha, M., Peter, A. H. G., Bullock, J. S., et al. 2013, MNRAS, 430, 81
Sales, L. V., Wetzel, A., & Fattahi, A. 2022, NatAs, 6, 897
Salucci, P. 2019, A&ARv, 27, 2
Salucci, P., Nesti, F., Gentile, G., & Martins, C. F. 2010, A&A, 523, A83
Sameie, O., Creasey, P., Yu, H.-B., et al. 2018, MNRAS, 479, 359
Sameie, O., Yu, H.-B., Sales, L. V., Vogelsberger, M., & Zavala, J. 2020, PhRvL, 124, 141102
Sameie, O., Boylan-Kolchin, M., Sanderson, R., et al. 2021, MNRAS, 507, 720
Samuel, J., Wetzel, A., Chapman, S., et al. 2021, MNRAS, 504, 1379
Sanderson, R. E., Garrison-Kimmel, S., Wetzel, A., et al. 2018, ApJ, 869, 12
Sanderson, R. E., Wetzel, A., Loebman, S., et al. 2020, ApJS, 246, 6
Santos-Santos, I. M. E., Navarro, J. F., Robertson, A., et al. 2020, MNRAS, 495, 58
Schutz, K., Lin, T., Safdi, B. R., & Wu, C.-L. 2018, PhRvL, 121, 081101
Schwab, C., Rakich, A., Gong, Q., et al. 2016, Proc. SPIE, 9908, 2220
Silverwood, H., & Easther, R. 2019, PASA, 36, e038
Spergel, D. N., & Steinhardt, P. J. 2000, PhRvL, 84, 3760
Teyssier, R. 2002, A&A, 385, 337
Tulin, S., & Yu, H.-B. 2018, PhR, 730, 1
van der Velden, E. 2020, JOSS, 5, 2004
Vargya, D., Sanderson, R., Sameie, O., et al. 2022, MNRAS, 516, 2389
Virtanen, P., Gommers, R., Oliphant, T. E., et al. 2020, NatMe, 17, 261
Vogelsberger, M., Zavala, J., & Loeb, A. 2012, MNRAS, 423, 3740
Vogelsberger, M., Zavala, J., Schutz, K., & Slatyer, T. R. 2019, MNRAS, 484, 5437
Wadsley, J. W., Keller, B. W., & Quinn, T. R. 2017, MNRAS, 471, 2357
Walker, M. G., & Penarrubia, J. 2011, ApJ, 742, 20
Weinberg, M. D. 1998, MNRAS, 299, 499
Weinberger, R., Springel, V., & Pakmor, R. 2020, ApJS, 248, 32
Wetzel, A., & Garrison-Kimmel, S., 2020a HaloAnalysis: Read and analyze halo catalogs and merger trees, Astrophysics Source Code Library, ascl:2002.014
Wetzel, A., & Garrison-Kimmel, S., 2020b GizmoAnalysis: Read and analyze Gizmo simulations, Astrophysics Source Code Library, ascl:2002.015
Wetzel, A., Hayward, C. C., Sanderson, R. E., et al. 2023, ApJS, 265, 44
Wright, J. T., & Robertson, P. 2017, RNAAS, 1, 51
Yoshida, N., Springel, V., White, S. D. M., & Tormen, G. 2000, ApJ, 544, L87
Zavala, J., Lovell, M. R., Vogelsberger, M., & Burger, J. D. 2019, PhRvD, 100, 063007